

Geophysical Research Letters®

RESEARCH LETTER

10.1029/2022GL101270

Special Section:

The Large Marsquake of Sol 1222

Key Points:

- The M_w 4.7 S1222a event is the first Marsquake large enough for multi-orbit surface wave location independent of a priori seismic velocity
- Using measurements of R1, R2, and R3 Rayleigh waves, we determine an epicentral distance consistent with that estimated from body waves
- Elliptical particle motion is observed for Rayleigh wave arrivals broadly consistent with the backazimuth identified from body waves

Supporting Information:

Supporting Information may be found in the online version of this article.

Correspondence to:

M. P. Panning,
Mark.P.Panning@jpl.nasa.gov

Citation:

Panning, M. P., Banerdt, W. B., Beghein, C., Carrasco, S., Ceylan, S., Clinton, J. F., et al. (2023). Locating the largest event observed on Mars with multi-orbit surface waves. *Geophysical Research Letters*, 50, e2022GL101270. <https://doi.org/10.1029/2022GL101270>

Received 28 SEP 2022

Accepted 20 DEC 2022

Author Contributions:

Conceptualization: M. P. Panning, M. Drilleau, S. C. Stähler

Formal analysis: M. P. Panning, C. Beghein, S. Carrasco, S. Ceylan, D. Kim, B. Knapmeyer-Endrun, J. Li

Funding acquisition: W. B. Banerdt

© 2022 The Authors.

This is an open access article under the terms of the [Creative Commons Attribution-NonCommercial License](https://creativecommons.org/licenses/by-nc/4.0/), which permits use, distribution and reproduction in any medium, provided the original work is properly cited and is not used for commercial purposes.

Locating the Largest Event Observed on Mars With Multi-Orbit Surface Waves

M. P. Panning¹, W. B. Banerdt¹, C. Beghein², S. Carrasco³, S. Ceylan⁴, J. F. Clinton⁴, P. Davis⁵, M. Drilleau⁵, D. Giardini⁴, A. Khan^{4,6}, D. Kim⁴, B. Knapmeyer-Endrun³, J. Li², P. Lognonné⁷, S. C. Stähler⁴, and G. Zenhäusern⁴

¹Jet Propulsion Laboratory, California Institute of Technology, Pasadena, CA, USA, ²University of California, Los Angeles, Los Angeles, CA, USA, ³University of Cologne, Cologne, Germany, ⁴Institute of Geophysics, ETH Zürich, Zürich, Switzerland, ⁵ISAE Supaero, Toulouse, France, ⁶Institute of Geochemistry and Petrology, ETH Zürich, Zürich, Switzerland, ⁷Université Paris Cité, Institut de physique du globe de Paris, CNRS, Paris, France

Abstract Prior to the 2018 landing of the InSight mission, the InSight science team proposed locating Marsquakes using multiple orbit surface waves, independent of seismic velocity models, for events larger than M_w 4.6. The S1222a M_w 4.7 of 4 May 2022 is the largest Marsquake recorded and the first large enough for this method. Group arrivals of the first three orbits of Rayleigh waves are determined to derive the group velocity, epicentral distance, and origin time. The mean distance of $36.9 \pm 0.3^\circ$ agrees with the Marsquake Service (MQS) distance based on body wave measurements of $37.0 \pm 1.6^\circ$. The origin time from surface waves is systematically later than the MQS origin time by 20 s. Backazimuth estimation is similar to body wave estimations from MQS although suggesting a shift to the south. Backazimuth estimates from R2 and R3 are more scattered, but do show clear elliptical motion.

Plain Language Summary Waves that move along the surface all the way around the planet of Mars can be used to figure out where a Marsquake occurred without knowing in advance how fast the waves move through the planet, because we know how big the planet is. Before InSight got to Mars, we predicted that we would be able to see these waves if an event was big enough, and on 4 May 2022, we finally saw a Marsquake large enough to test this approach. Based on the timing of the arrivals of these waves, we were able to figure out the distance and timing of the Marsquake. The results agreed well with the approach we had been using for smaller events, giving us additional confidence in our tools for figuring out where Marsquakes have happened.

1. Introduction

On 4 May 2022, the 1222nd sol of the InSight mission (Banerdt et al., 2020), the SEIS instrument (Lognonné et al., 2019) recorded the largest event of the mission to date, called S1222a (Kawamura et al., 2022). The moment magnitude of the event is estimated as M_w 4.7, meaning it is approximately five times larger in terms of seismic moment than the second largest observed event (S0976a, Horleston et al., 2022). The large moment release of this event has opened up a variety of new observations not possible with previous smaller events.

In particular, this event is the first that allows us to test a single station location method proposed before the launch of the mission that makes use of the observation of multiple orbit surface waves (Khan et al., 2016; Panning et al., 2015). Prior to the mission, there was concern about how well the mission could locate events with a single station when the seismic velocity structure of Mars was not well-known in advance. While *a priori* models of the interior velocity structure were available before landing (e.g., Bagheri et al., 2019; Khan et al., 2018; Smrekar et al., 2019) and body wave location methods that depend on the initially unknown velocity structure have been successful in locating events (Durán et al., 2022), proposing a method that did not directly depend on any knowledge of the velocity structure (beyond assuming the structure is spherically symmetric) allowed for a plan to verify locations based on body waves.

Multiple orbit surface waves have paths around the sphere of a planet that allow for multiple arrivals in the minutes and hours after the origin time of the event. For Rayleigh waves, recorded on the vertical and horizontal component in the great-circle plane connecting the source and receiver, we refer to these as R1, R2, R3, etc. R1 represents surface wave energy that takes the shortest distance around the planet (or minor arc) to the station,

Investigation: M. P. Panning, C. Beghein, S. Carrasco, S. Ceylan, J. F. Clinton, D. Kim, B. Knapmeyer-Endrun, J. Li, S. C. Stähler

Methodology: M. P. Panning, C. Beghein, S. Carrasco, S. Ceylan, J. F. Clinton, P. Davis, M. Drilleau, A. Khan, D. Kim, B. Knapmeyer-Endrun, J. Li, P. Lognonné

Project Administration: M. P. Panning, W. B. Banerdt, D. Giardini, P. Lognonné

Software: M. P. Panning, P. Davis, D. Kim, B. Knapmeyer-Endrun, J. Li, G. Zenhäusern

Supervision: C. Beghein, D. Giardini, P. Lognonné

Visualization: G. Zenhäusern

Writing – original draft: M. P. Panning, C. Beghein, S. Carrasco, P. Davis, D. Kim, B. Knapmeyer-Endrun, J. Li

Writing – review & editing: M. P. Panning, C. Beghein, S. Carrasco, J. F. Clinton, P. Davis, M. Drilleau, A. Khan, D. Kim, B. Knapmeyer-Endrun, J. Li, P. Lognonné, S. C. Stähler

while R2 propagates away from the source 180° away from the direction of R1 and takes the longer path around the planet (or major arc). R3 follows the minor arc, but has an additional full circuit around the planet compared to R1. If we assume a spherically symmetric model of velocity structure, because R3 and R1 differ only by the complete trip around the planet, we are able to determine the velocity of surface wave propagation and therefore also the epicentral distance and origin time without knowing the velocity in advance (Panning et al., 2015). A set of three equations determines the three unknowns as

$$U = \frac{2\pi}{t_{R3} - t_{R1}} \quad (1)$$

$$\Delta = \pi - \frac{1}{2}U(t_{R2} - t_{R1}) \quad (2)$$

$$t_0 = t_{R1} - \frac{\Delta}{U}, \quad (3)$$

where t_{R1} , t_{R2} , and t_{R3} are the arrival times of the multi-orbit Rayleigh waves, U is the great-circle average group velocity of the Rayleigh wave (in radians per second measured on the great circle), and Δ and t_0 are the epicentral distance and origin time of the event, respectively. In addition to epicentral distance and origin time, the full event location also requires an estimation of the backazimuth, and this can be obtained from the elliptical particle motion of the Rayleigh waves (see Section 3).

In order for this method to be used, however, an event needs to be large enough so that R3 can be observed. On Earth, R3 can be reliably observed at quiet stations by M_w 5.5–6, but Panning et al. (2015) argued that with the smaller radius of Mars, R3 should be reliably observable around M_w 4.6 on Mars for a vertical instrument noise of 10^{-9} m/s²/Hz^{1/2} in the surface wave bandwidth. With the estimates of Martian seismicity available at the time, 1–10 events of M_w 5.3 were predicted over the course of the mission, and so it was expected that this method could be applied to several of the largest events observed by InSight. In reality, both the daily wind-induced noise that is much larger than 10^{-9} m/s²/Hz^{1/2} (e.g., Lognonné et al., 2020) and a seismicity generating mostly $M_w < 4$ events (Brinkman et al., 2021; Ceylan et al., 2022; Clinton et al., 2020; Giardini et al., 2020; Jacob et al., 2022) has made this method impossible for events prior to S1222a. This was, therefore, the first event that exceeded the pre-mission estimated magnitude threshold, and it provides an excellent test case for the method at last.

2. Measuring Multi-Orbit Rayleigh Wave Arrival Times

Panning et al. (2015) and Khan et al. (2016) proposed a straightforward approach to picking the t_{R1} to t_{R3} arrival times and demonstrated it using terrestrial and synthetic Martian data (called Method 1 in following figures), respectively. As illustrated in Figure 1, a series of narrow-band filters of the data (InSight Mars SEIS Data Service, 2019) are performed on center frequencies spaced in 15% intervals. For each center frequency, zero-phase (i.e., two pass) 2nd-order Butterworth bandpass filtering with a width of 30% of the central frequency was performed with ObsPy software (Krischer et al., 2015), and then the envelope was calculated, and picks were made in frequency bands where a clear peak was observable. In the frequency band between 0.01 and 0.1 Hz, where we looked for surface wave energy, the raw data shows evidence of many glitches common to InSight data (e.g., Ceylan et al., 2021; Kim et al., 2021; Scholz et al., 2020). In particular, a large glitch arrives close to the R3 arrival time, and so all measurements are made on deglitched data. Deglitching of the event data was carried out with the UCLA method (with more recent modifications; see Supporting Information S1) described in Scholz et al. (2020) on raw 20 samples per second velocity channels BHU, BHV, BHW with an additional step to identify glitches hidden in the event coda that show up as steps in displacement.

Four different methods that differ in the precise filter definition and picking method are used for picking t_{R1} – t_{R3} to be confident in the location determined, with Method 1 described above. Method 2 is a similar approach performed routinely by the Marsquake Service (MQS; Clinton et al., 2018) on half-octave wide frequency bands and uses the arrival times included in their standard catalog (InSight Marsquake Service, 2022). Common picks for each of t_{R1} – t_{R3} are only possible for periods between 28 and 34s. This method was tested and found to be effective in a pre-mission blind test (Clinton et al., 2017; van Driel et al., 2019). Method 3 is a multiple filter technique implemented in the Computer Programs in Seismology (Herrmann, 2013) to calculate the envelope energy on the vertical component of the seismogram, and the preferred arrival time corresponds to the maximum

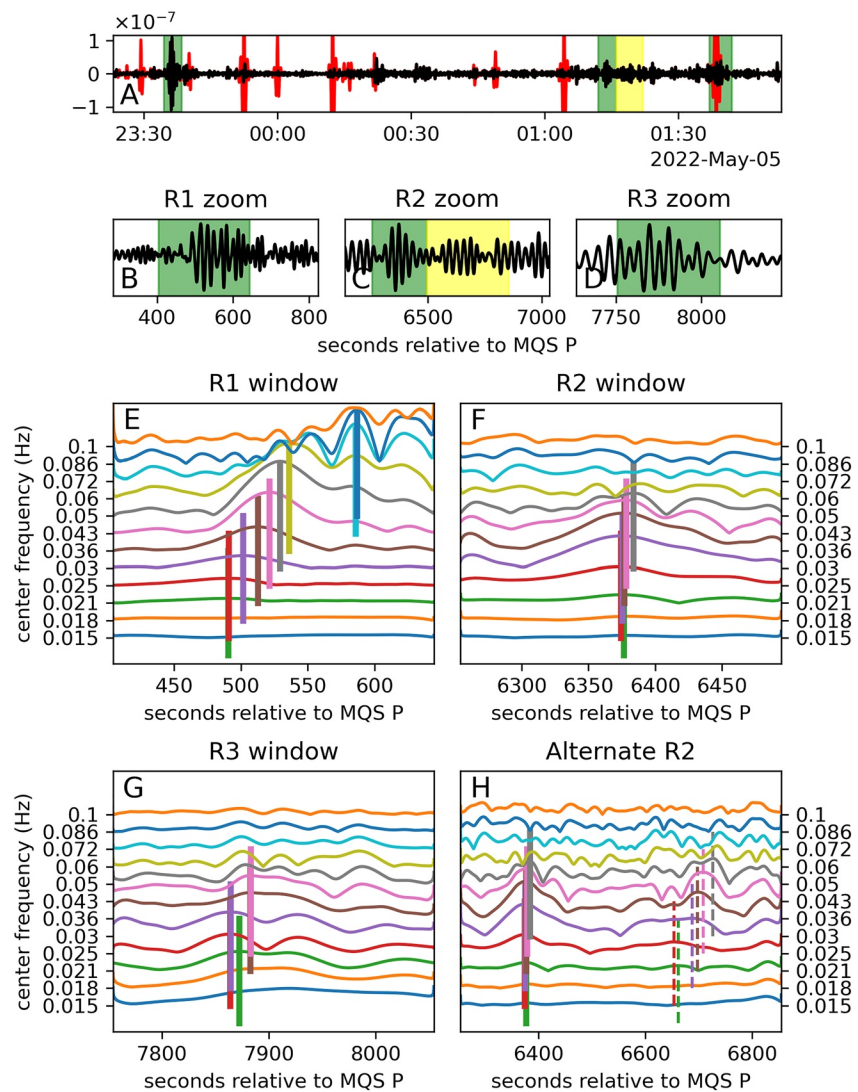


Figure 1. (a) 2.5 hr of raw (red) and deglitched (black) vertical component data starting with the MQS origin time of 23:23:06.57 UTC on 4 May 2022, bandpass filtered between 0.02 and 0.05 Hz. (b) Zoom into the R1 arrival window bandpass filtered between 0.02 and 0.09 Hz with the window for the set of narrow-band filters shown in panel D highlighted in green. (c) and (d) Zoom window showing R2 and R3 arrival times, respectively, filtered between 0.02 and 0.04 Hz. The green boxes highlight the windows for filter banks in panels F and G, while the yellow box indicates the additional R2 window considered in panel (h) (e)–(h) Filter banks where the central frequency of each trace is shown on the left where all traces are bandpassed within a window extending 30% from the central frequency. Picks for Method 1 are shown with vertical bars where the color indicates which frequency band the pick was made on. Dashed lines in (h) show the alternate R2 arrival time picks discussed in the text.

energy at different periods and time windows. For R1, picks are made for periods from 16.3 to 40.9 s, but picks for R1–R3 are only available for periods from 25.3 to 34.6 s. Method 4 derived arrival times at periods between 39 and 19 s by applying the multiple filter technique (Dziewonski et al., 1969) in the implementation of Meier et al. (2004) to the vertical-component seismogram and, for each period, picking the amplitude maxima in time windows around the R1, R2, and R3 phases.

While R1 shows clear dispersion, which can be used to model seismic structure along the minor arc as a function of depth, the picks for both R2 and R3 are visible over a much narrower frequency band, and show little or no dispersion. Because of this lack of dispersion and the presence of other potential signals of similar amplitude near the preferred R2 observation, we also consider a second window for R2. The alternate R2 arrives roughly 300 s later (Figure 1g), and shows potential evidence of dispersion. However, this interpretation is not favored. The

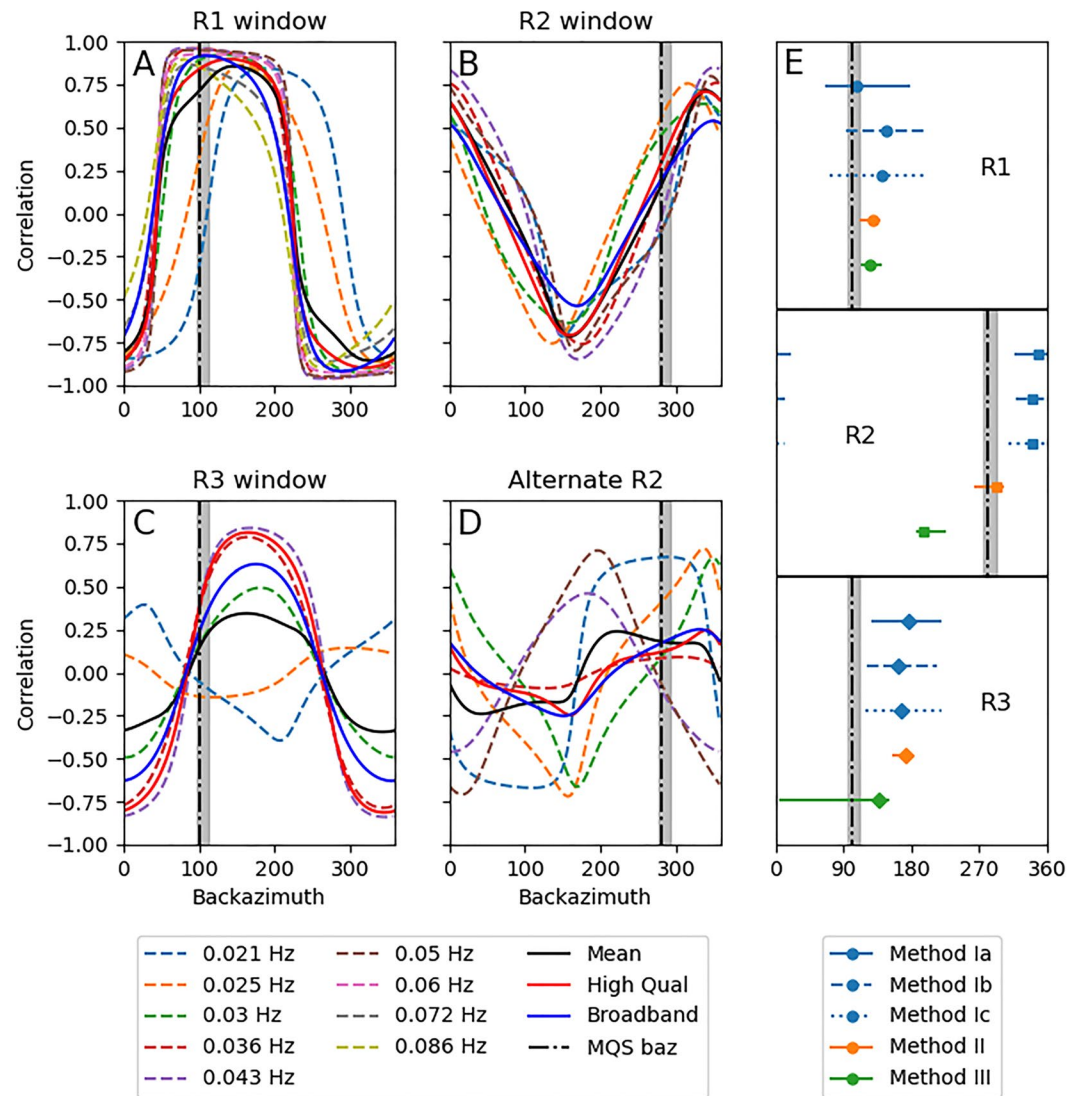


Figure 2. Backazimuth estimation for each Rayleigh wave arrival. For each backazimuth, correlation is calculated between the horizontal component positive in the direction of the proposed backazimuth and the Hilbert transform of the vertical component. Correlations are calculated on narrow band waveforms in time windows centered on the pick times shown in Figure 1 with a width of 4 dominant periods. For the broadband waveforms, correlations are calculated over 200 s windows beginning at 450 s after the P arrival time for R1 (a), 6,250 s for R2 (b), 7,825 s for R2 (c), and 6,550 s for the alternate R2 time (d). (e) Summary of backazimuth determined from R1, R2, and R3. Methods Ia–Ic are based on the results shown in panels (a)–(d) for the broadband, mean over the frequency bands, and average over the high quality measurements, respectively. Methods II and III are independent approaches described in the text. In all panels, the MQS backazimuth is shown with the dot-dash line with uncertainty shaded in gray.

envelopes in this time window are complicated with multiple peaks, and this pick suggests a location significantly closer (roughly 8°) than that determined by MQS using the body wave timing (Kawamura et al., 2022). Additionally, the waveforms in different frequency bands do not show consistent elliptical polarization with no clear relationship to the backazimuth estimated from the MQS body wave polarization (Figure 2d). For this reason, we use the R2 arrival times as shown in Figure 1e.

Using the travel times estimated in narrow frequency band windows, we can use all frequency bands for which we can pick $t_{R1} - t_{R3}$ to estimate the epicentral distance and origin time using Equations 1–3. These results as well as the estimated great-circle average Rayleigh wave group velocity are shown for all four methods of picking group arrivals in Figure 3. For each method, the standard deviation across the different frequency band estimates is shown. The summary value is defined by the average across the different picking methods and the standard

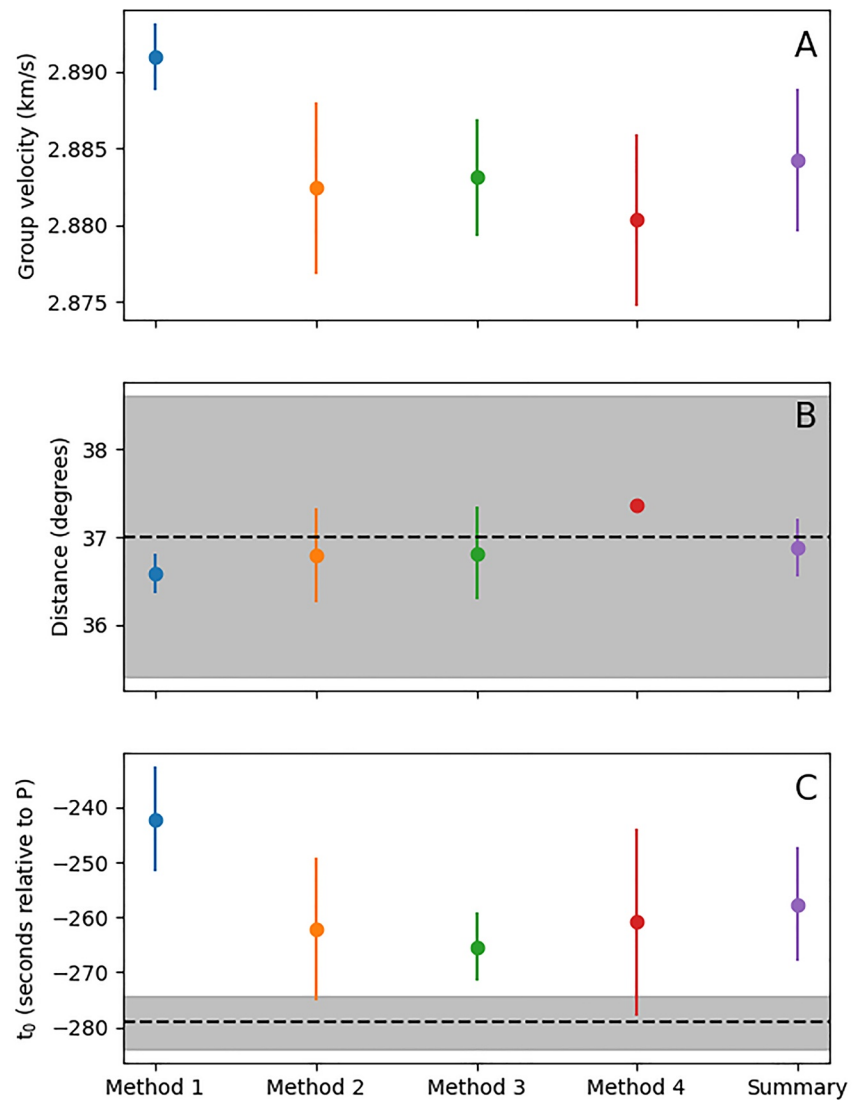


Figure 3. For each of the four methods employed, the average value and standard deviation across the individual narrow band frequencies measured is shown for the group velocity (a), epicentral distance (b), and origin time (c) calculated from Equations 1–3. Dashed black lines represent the MQS estimated epicentral distance and origin time (Kawamura et al., 2022), while the gray shaded box represents error bounds from Kawamura et al. (2022).

deviation of those methods. For epicentral distance and origin time, these are compared with the MQS estimates from body wave observations shown with shading to indicate the uncertainty defined by the MQS method, described in more detail in Kawamura et al. (2022).

3. Rayleigh Wave Ellipticity and Backazimuth Estimation

In Panning et al. (2015), backazimuth estimation using Rayleigh wave energy on Earth events was performed using both a broadband window over all measured frequency bands, as well as averaging the narrow band backazimuth estimations with similar accuracy, although the broadband estimation showed slightly smaller mismatch across the events studied. For each prospective backazimuth in Figure 2, we rotate a horizontal component such that motion along that backazimuth pointing toward the prospective source is positive. Correlation is calculated with the Hilbert transform of the vertical component, and should reach a maximum at the correct backazimuth. Note that this convention for the horizontal component is the opposite of the radial component of the standard seismological ZRT coordinate system which is defined positive in the direction from source to receiver, which would be

negatively correlated with the Hilbert-transformed vertical component for standard retrograde elliptical Rayleigh wave particle motion. The narrowness of the correlation peak, however, was strongly dependent on the presence or absence of Love wave energy in the measurement window (Panning et al., 2015). While Love wave energy is seen for this event (Beghein et al., 2022; Kawamura et al., 2022; Kim, Stähler, et al., 2022; Li et al., 2022), it arrives in a non-overlapping time window with the Rayleigh energy, and so estimated correlation peaks are generally broad (Figure 2). In Figure 2e, we show three backazimuths from this correlation-based method (Methods Ia-Ic), which correspond to the correlation computed over broadband data, the average over all narrow-band data, and only over “high-quality” data. Note that we number the different approaches to back-azimuth estimation with Roman numerals to differentiate from the different surface wave arrival estimations numbered with Arabic numerals. High-quality data excludes measurement windows which do not have clear peaks or have multiple peaks of similar amplitude in the enveloped data (see Table S1 in Supporting Information S1 for specific frequencies identified as lower quality). In each case, the range of possible backazimuths shown in Figure 2 represent the range with correlation above 80% of the maximum value. We also show estimates for two additional methods. Method II is based on the maximization of the ground-motion amplitudes on the Z and R components around the arrival time of the Rayleigh waves for different frequencies. The preferred back-azimuths are derived from the maximum of the $Z \times R/T$ coefficient, which is computed from seismogram envelopes. This method has a 180° uncertainty, which is resolved by assessing the phase shift between the Z and R components, obtained from their maximum cross-correlation. The back-azimuth of each Rayleigh wave is the median obtained from the frequencies for which Rayleigh energy is observed and for which mainly retrograde motion is determined (phase shift > 0). See Carrasco et al. (2022) for details. Method III uses several independent approaches to obtain frequency-dependent polarization and backazimuth estimates of surface wave arrivals. This method has been previously implemented to extract seismic signals that are strongly elliptically polarized and traveling along the great circle path, leading to the first detection of Rayleigh waves on Mars (Kim, Banerdt, et al., 2022). See Kim, Stähler, et al. (2022) for details.

The broadband estimation of the correlation for R1 (Method Ia), as well as Methods II and III peak close to the MQS backazimuth determined using body waves (solid blue line in Figure 2a), but the averages over the narrowband estimates (Methods Ib and Ic) have a broad peak that reach a maximum value $30\text{--}40^\circ$ to the south of the MQS estimate. With the much lower signal to noise ratio (SNR) for R2, the backazimuths are more variable between methods with Methods Ia-Ic shifted significantly to the north, while Method III is shifted to the west, but the methods do bracket the predicted azimuth from the MQS body wave event azimuth. On the other hand, the potential alternate R2 time, which shows more apparent dispersion than the preferred R2 arrival, does not show strong correlation peaks indicating elliptical particle motion, and the weak peaks that are observed show no consistency between different frequency bands. This strongly supports that this window does not contain the major R2 energy, and thus should not be used for location or structure estimation. Finally, the R3 backazimuth estimates are shifted to the south for all five methods considered, but SNR is fairly low for this observation, and the fact that elliptical motion does seem to be resolved in all methods at least gives credence to interpreting this arrival as R3. It is, however, important to note that S1222a occurs during the noisy season on Mars, and therefore the SNR for R2 and R3 are low. Both ellipticity and backazimuth estimations are more challenging and can be biased in this situation as wind effects can mimic the elliptical motion of Rayleigh waves or even generate surface waves at different azimuths (e.g., Stutzmann et al., 2021). This may contribute to both the offset of these backazimuth estimates from the MQS backazimuth as well as the scatter between the different methods.

4. Results

The epicentral distance determined for all the sets of surface wave arrival times is 36.9° with a standard deviation of 0.3° . Note that this standard deviation represents only the variation of distance estimates based on different surface wave measurement approaches, and likely underestimates the total uncertainty in distance which should also include additional uncertainty due to 3D variation in seismic velocity, or possible biases in the measured surface wave arrival times due to effects such as interference with removed glitches. This estimate is in good agreement with the body-wave based MQS value. All surface wave estimates are within the uncertainty bounds obtained by the MQS ($37 \pm 1.6^\circ$) (Kawamura et al., 2022), while the MQS estimate agrees within one standard deviation with the mean surface wave epicentral distance calculated across different methods.

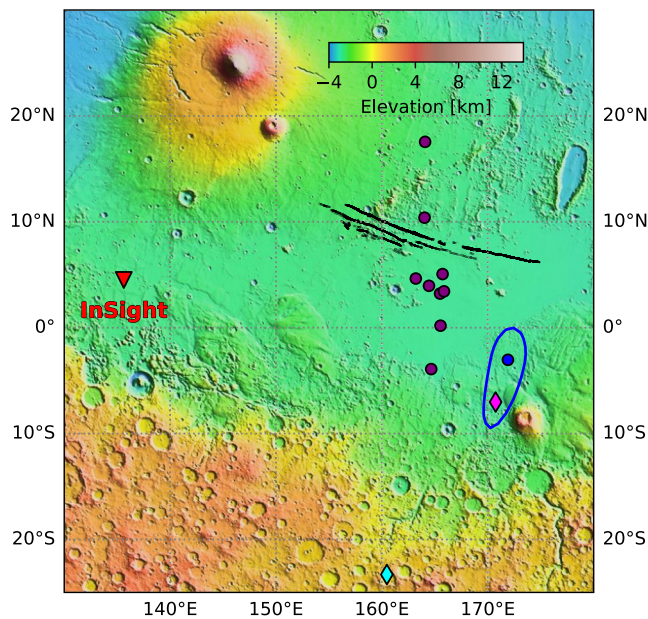


Figure 4. Estimated locations of S1222a from MQS (Kawamura et al., 2022, blue circle with uncertainty shown with blue ellipse), based on the multi-orbit distance estimation and the backazimuth estimated from the broadband polarization of R1 (magenta diamond), and based on the backazimuth estimated from the average of the correlation functions across the high-quality narrow band frequency estimates (cyan diamond). Purple dots show other events located by MQS. Figure is adapted from Kawamura et al. (2022).

The backazimuth estimated from the R1 broadband measurement of 108° is consistent with the MQS backazimuth uncertainty bounds (96°–112°). However, if the average over the high quality narrow band estimates is used instead (which provided similar accuracy for the Earth data analyzed in Panning et al. (2015)), the 32° mismatch in backazimuth calculation (108 for the broadband vs. 140 for the average over high quality narrow band estimates) is outside the uncertainty bounds estimated by the MQS. When combining the distance and backazimuth estimates, the location using the broadband backazimuth estimate is offset from the nominal MQS location by ~4° (Figure 4, magenta diamond), while backazimuth based on the average across measurements leads to location that differs from the nominal MQS location by ~23° (Figure 4, cyan diamond) which is well outside the estimated uncertainty of the MQS location (blue dot and ellipse in Figure 4).

The origin time determination for all surface wave methods is roughly 20 s later than the MQS origin time estimate. Some possible explanations for the mismatch between estimated origin time are considered in the Discussion section. An offset of origin time of 20 s is also quite consistent with the range of offsets observed for Earth events located with this method by Panning et al. (2015) which were generally offset from catalog origin times within ± 30 s. Additionally, that study showed that origin time offsets compared with catalog origin time often significantly exceeded the standard deviation of origin time estimates across different frequency bands, so the lack of overlap of the standard deviations in Figure 3c with the MQS t_0 should not be surprising.

5. Discussion

The results show close agreement in distance estimation between the MQS body wave determination and that derived from the multi-orbit surface waves, which do not depend on a priori velocity models, beyond the assumption of spherical symmetry. This provides important validation of the MQS method that has been utilized for many events now and performed well. The MQS body wave method's success includes accurately providing location estimates for impacts within 300 km of the lander in order to target HiRISE images showing new craters (Garcia et al., 2022) as well as larger, more distant impacts with craters detected by the CTX camera aboard MRO (Posiolova et al., 2022). However, the difficulty in matching backazimuth between P- and surface waves shows that the latter may be affected by off-great-circle propagation due to three-dimensional (3D) structure, particularly as this path does cross the dichotomy between the northern and southern hemispheres of Mars at a relatively shallow angle. R2 and R3 backazimuths also show apparent offsets from the MQS backazimuth, but these are in general much more poorly resolved due to lower SNR (e.g., Kim, Stähler, et al., 2022). The t_0 mismatch may also be related to 3D structure. For example, if the R1 path were a little slower than the great-circle average group velocity, one might expect that the R1 would arrive a little late, and thus a t_0 estimated from Equation 3, would be correspondingly late. If we look at measured arrival times near 0.03 Hz, and we assume the MQS location and origin time is correct and all surface wave propagation is along the great circle path, the velocity of R2 is ~0.7% faster than R1. However, the great-circle average velocity calculated as the path-length weighted average of the R1 and R2 velocities is ~0.4% slower than the great-circle averaged velocity computed from the difference between t_{R3} and t_{R1} , suggesting that we cannot simply explain the difference between estimated origin times through assuming the MQS origin time is correct and all differences in the surface wave estimation is due to different minor arc and major arc velocity. Likely the true explanation relates to some combination of differences in minor and major arc velocity, offsets in true distance and origin time within the uncertainties of the MQS estimates, and possible small biases in the estimates of $t_{R3} - t_{R1}$, as may happen due to interference from glitches or other causes.

6. Conclusion

Consistent with pre-mission expectations on observability of surface waves circling Mars, the $M_w 4.7$ S1222a Marsquake was large enough to make observations of multiple-orbit Rayleigh waves. These were used to apply a location method that does not depend on *a priori* velocity structure, and the recovered distance and broadband backazimuth estimate agree well with the standard MQS body-wave based approach, providing additional verification of the location approach used for the bulk of events observed in the InSight mission.

Data Availability Statement

All raw waveform data is available through the InSight Mars SEIS Data Service @ IPGP, IRIS-DMC and NASA PDS (InSight Mars SEIS Data Service, 2019). All processed data and processing codes used in this study are available through https://github.com/mpanning/R1R2R3_data_codes with the release v1.0 preserved with <https://doi.org/10.5281/zenodo.7469298>.

Acknowledgments

We acknowledge NASA, CNES, their partner agencies and Institutions (UKSA, SSO, DLR, JPL, IPGP-CNRS, ETHZ, IC, MPS-MPG) and the flight operations team at JPL, SISMOC, MSDS, IRIS-DMC, and PDS for providing SEED SEIS data. M.P.P. and W.B.B. were supported by the NASA InSight mission and funds from the Jet Propulsion Laboratory, California Institute of Technology, under a contract with the National Aeronautics and Space Administration (80NM0018D0004). French co-authors acknowledge the French Space Agency CNES and ANR (ANR-19-CE31-0008-08; ANR-18-IDEX-0001). C.B. and J.L. were funded by NASA InSight PSP Grant 80NSSC18K1679. Marsquake Service (MQS) operations at ETH are supported by ETH Research grant ETH-06 17-02. ETH authors recognize support from the ETH + funding scheme (ETH+02 19-1: Planet Mars). This is InSight contribution ICN 275. © 2022. All rights reserved.

References

- Bagheri, A., Khan, A., Al-Attar, D., Crawford, O., & Giardini, D. (2019). Tidal response of Mars constrained from laboratory-based viscoelastic dissipation models and geophysical data. *Journal of Geophysical Research: Planets*, 124(11), 2703–2727. <https://doi.org/10.1029/2019je006015>
- Banerdt, W. B., Smrekar, S., Banfield, D., Giardini, D., Golombek, M., Johnson, C., et al. (2020). Initial results from the InSight mission on Mars. *Nature Geoscience*, 13(3), 183–189. <https://doi.org/10.1038/s41561-020-0544-y>
- Beghein, C., Li, J., Weidner, E., Maguire, R., Wookey, J., Lekic, V., et al. (2022). Crustal anisotropy in the Martian lowlands from surface wave. *Geophysical Research Letters*, 49(24), e2022GL101508. <https://doi.org/10.1029/2022GL101508>
- Beghein, C., Snoke, J., & Fouch, M. (2010). Depth constraints on azimuthal anisotropy in the Great Basin from Rayleigh-wave phase velocity maps. *Earth and Planetary Science Letters*, 289(3–4), 467–478. <https://doi.org/10.1016/j.epsl.2009.11.036>
- Brinkman, N., Stähler, S. C., Giardini, D., Schmeltzbach, C., Khan, A., Jacob, A., et al. (2021). First focal mechanisms of Marsquakes. *Journal of Geophysical Research: Planets*, 126(4), e2020JE006546. <https://doi.org/10.1029/2020JE006546>
- Carrasco, S., Knapmeyer-Endrun, B., Margerin, L., Xu, Z., & Charalambous, C. (2022). Crustal Martian structure from the analysis and inversion of large-Marsquakes Rayleigh waves ellipticity. *American Geophysical Union Fall Meeting 2022*.
- Ceylan, S., Clinton, J. F., Giardini, D., Böse, M., Charalambous, C., van Driel, M., et al. (2021). Companion guide to the Marsquake catalog from InSight, sols 0–478: Data content and non-seismic events. *Physics of the Earth and Planetary Interiors*, 310, 106597. <https://doi.org/10.1016/j.pepi.2020.106597>
- Ceylan, S., Clinton, J. F., Giardini, D., Stähler, S. C., Horleston, A., Kawamura, T., et al. (2022). The Marsquake catalogue from InSight, sols 0–1011. *Physics of the Earth and Planetary Interiors*, 333, 106943. <https://doi.org/10.1016/j.pepi.2022.106943>
- Clinton, J. F., Ceylan, S., van Driel, M., Giardini, D., Stähler, S. C., Böse, M., et al. (2020). The Marsquake catalog from InSight, sols 0–478. *Physics of the Earth and Planetary Interiors*, 310, 106595. <https://doi.org/10.1016/j.pepi.2020.106595>
- Clinton, J. F., Giardini, D., Böse, M., Ceylan, S., van Driel, M., Euchner, F., et al. (2018). The Marsquake Service: Securing daily analysis of SEIS data and building the Martian seismicity catalogue for InSight. *Space Science Reviews*, 214(8), 133. <https://doi.org/10.1007/s11214-018-0567-5>
- Clinton, J. F., Giardini, D., Lognonné, P., Banerdt, W. B., van Driel, M., Drilleau, M., et al. (2017). Preparing for InSight: An invitation to participate in a blind test for Martian seismicity. *Seismological Research Letters*, 88(5), 1290–1302. <https://doi.org/10.1785/0220170094>
- Durán, C., Khan, A., Ceylan, S., Charalambous, C., Kim, D., Drilleau, M., et al. (2022). Observation of a core-diffracted P-wave from a farside impact with implications for the lower-mantle structure of Mars. *Geophysical Research Letters*, 49(21), e2022GL100887. <https://doi.org/10.1029/2022GL100887>
- Dziewonski, A., Bloch, S., & Landisman, M. (1969). A technique for the analysis of transient seismic signals. *Bulletin of the Seismological Society of America*, 59(1), 427–444. <https://doi.org/10.1785/bssa0590010427>
- García, R. F., Daubar, I. J., Beucler, E., Posiolova, L., Lognonné, P., Rolland, L., et al. (2022). Newly formed craters on Mars located using seismic and acoustic wave data from InSight. *Nature Geoscience*, 15(10), 774–780. <https://doi.org/10.1038/s41561-022-01014-0>
- Giardini, D., Lognonné, P., Banerdt, W. B., Christensen, U., Clinton, J., van Driel, M., et al. (2020). The seismicity of Mars. *Nature Geoscience*, 13, 205–212. <https://doi.org/10.1038/s41561-020-0539-8>
- Herrmann, R. B. (2013). Computer programs in seismology: An evolving tool for instruction and research. *Seismological Research Letters*, 84(6), 1081–1088. <https://doi.org/10.1785/0220110096>
- Horleston, A. C., Clinton, J. F., Ceylan, S., Giardini, D., Charalambous, C., Irving, J. C. E., et al. (2022). The far side of Mars: Two distant Marsquakes detected by InSight. *The Seismic Record*, 2(2), 88–99. <https://doi.org/10.1785/0320220007>
- InSight Marsquake Service. (2022). *Mars seismic catalogue, InSight mission; v12 2022-10-01 (version 12.0)*. ETHZ, IPGP, JPL, ICL, University. <https://doi.org/10.12686/a18>
- InSight Mars SEIS Data Service. (2019). Seis raw data, InSight mission. IPGP, JPL, CNES, ETHZ, ICL, MPS, ISAE-Supaero, LPG, MFSC. https://doi.org/10.18715/seis.insight.xb_2016
- Jacob, A., Plasman, M., Perrin, C., Fuji, N., Lognonné, P., Xu, Z., et al. (2022). Seismic sources of InSight Marsquakes and seismotectonic context of Elysium Planitia, Mars. *Tectonophysics*, 837, 229434. <https://doi.org/10.1016/j.tecto.2022.229434>
- Kawamura, T., Clinton, J. F., Zenhäusern, G., Ceylan, S., Horleston, A. C., Dahmen, N. L., et al. (2022). Largest Marsquake ever detected by InSight: S1222a. *Geophysical Research Letters*, 49, e2022GL101543. <https://doi.org/10.1029/2022GL101543>
- Khan, A., Liebske, C., Rozel, A., Rivoldini, A., Nimmo, F., Connolly, J. A. D., et al. (2018). A geophysical perspective on the bulk composition of Mars. *Journal of Geophysical Research: Planets*, 123(2), 575–611. <https://doi.org/10.1002/2017JE005371>
- Khan, A., van Driel, M., Böse, M., Giardini, D., Ceylan, S., Yan, J., et al. (2016). Single-station and single-event Marsquake location and inversion for structure using synthetic Martian waveforms. *Physics of the Earth and Planetary Interiors*, 258, 28–42. <https://doi.org/10.1016/j.pepi.2016.05.017>

- Kim, D., Banerdt, W. B., Ceylan, S., Giardini, D., Lekić, V., Lognonné, P., et al. (2022). Surface waves and crustal structure on Mars. *Science*, 378, 417–421. <https://doi.org/10.1126/science.abq7157>
- Kim, D., Stähler, S. C., Ceylan, S., Lekic, V., Maguire, R., Zenhäusern, G. (2022). Structure along the Martian dichotomy constrained by surface waves. *Geophysical Research Letters*. <https://doi.org/10.1029/2022GL101666>
- Kim, D., Davis, P., Lekić, V., Maguire, R., Compaire, N., Schimmel, M., et al. (2021). Potential pitfalls in the analysis and structural interpretation of seismic data from the Mars InSight mission. *Bulletin of the Seismological Society of America*, 111(6), 2982–3002. <https://doi.org/10.1785/0120210123>
- Krischer, L., Megies, T., Barsch, R., Beyreuther, M., Lecocq, T., Caudron, C., & Wasserman, J. (2015). ObsPy: A bridge for seismology into the scientific Python ecosystem. *Computational Science & Discovery*, 8(1), 014003. <https://doi.org/10.1088/1749-4699/8/1/014003>
- Li, J., Beghein, C., Panning, M. P., Davis, P., Lognonné, P., Banerdt, W. B., et al. (2022). Different Martian crustal seismic velocities across the dichotomy boundary from multi-orbiting surface waves. *Geophysical Research Letters*, 49, e2022GL101243. <https://doi.org/10.1029/2022GL101243>
- Lognonné, P., Banerdt, W. B., Giardini, D., Pike, W. T., Christensen, U., Laudet, P., et al. (2019). SEIS: The seismic experiment for internal structure of InSight. *Space Science Reviews*, 215(1), 12. <https://doi.org/10.1007/s11214-018-0574-6>
- Lognonné, P., Banerdt, W. B., Pike, W. T., Giardini, D., Christensen, U., Garcia, R. F., et al. (2020). Constraints on the shallow elastic and anelastic structure of Mars from InSight seismic data. *Nature Geoscience*, 13(3), 213–220. <https://doi.org/10.1038/s41561-020-0536-y>
- Meier, T., Dietrich, K., Stöckhert, B., & Harjes, H.-P. (2004). One-dimensional models of shear wave velocity for the eastern mediterranean obtained from the inversion of Rayleigh wave phase velocities and tectonic implications. *Geophysical Journal International*, 156(1), 45–58. <https://doi.org/10.1111/j.1365-246x.2004.02121.x>
- Panning, M. P., Beucler, E., Drilleau, M., Mocquet, A., Lognonné, P., & Banerdt, W. B. (2015). Verifying single-station seismic approaches using Earth-based data: Preparation for data return from the InSight mission to Mars. *Icarus*, 248, 230–242. <https://doi.org/10.1016/j.icarus.2014.10.035>
- Posiolova, L. V., Lognonné, P., Banerdt, W. B., Clinton, J. F., Collins, G. S., Kawamura, T., et al. (2022). Largest recent impact craters on Mars: Orbital imaging and surface seismic co-investigation. *Science*, 378(6618), 412–417. <https://doi.org/10.1126/science.abq7704>
- Scholz, J.-R., Widmer-Schmidrig, R., Davis, P., Lognonné, P., Pinot, B., Garcia, R. F., et al. (2020). Detection, analysis, and removal of glitches from InSight's seismic data from Mars. *Earth and Space Science*, 7(11), e2020EA001317. <https://doi.org/10.1029/2020EA001317>
- Smrekar, S. E., Lognonné, P., Spohn, T., Banerdt, W. B., Breuer, D., Christensen, U., et al. (2019). Pre-mission InSights on the interior of Mars. *Space Science Reviews*, 215(1), 3. <https://doi.org/10.1007/s11214-018-0563-9>
- Stutzmann, E., Schimmel, M., Lognonné, P., Horleston, A., Ceylan, S., van Driel, M., et al. (2021). The polarization of ambient noise on Mars. *Journal of Geophysical Research: Planets*, 126(1), e2020JE006545. <https://doi.org/10.1029/2020JE006545>
- van Driel, M., Ceylan, S., Clinton, J. F., Giardini, D., Alemany, H., Allam, A., et al. (2019). Preparing for InSight: Evaluation of the blind test for Martian seismicity. *Seismological Research Letters*, 90(4), 1518–1534. <https://doi.org/10.1785/0220180379>